Cement with bacterial nanocellulose cured at reservoir temperature: Mechanical performance in the context of CO2 geological storage

Juan Cruz Barría, Diego Manzanal, Patricia Cerruti, Jean-Michel Pereira

Cement with bacterial nanocellulose cured at reservoir temperature: mechanical performance in the context of CO_2 geological storage

Juan Cruz Barría[1,5], Diego Manzanal[1,2,*], Patricia Cerruti[3,4], Jean-Michel Pereira[5]

[1] Facultad de Ingeniería, Universidad Nacional de la Patagonia San Juan Bosco, 9004 Comodoro Rivadavia, Chubut, Argentina.

[2] E.T.S.I. Caminos, Universidad Politécnica de Madrid, Prof. Aranguren 3, 28040 Madrid, Spain.

[3] Instituto de Tecnología en Polímeros y Nanotecnología (ITPN), Grupo de Biotecnología y Materiales Biobasados, Universidad de Buenos Aires (UBA), CONICET, Facultad de Ingeniería, Las Heras 2214 (1127), Buenos Aires, Argentina.

[4] Universidad de Buenos Aires, Facultad de Ingeniería, Departamento de Ingeniería Química, Av. Intendente Güiraldes 2620 (1428) – Pabellón de Industrias, Ciudad Universitaria, Buenos Aires, Argentina.

[5] Navier, Ecole des Ponts, Univ Gustave Eiffel, CNRS, Marne-la-Vallée, France.

*Correspondence to d.manzanal@upm.es

Abstract

Storing CO_2 in deep underground reservoirs is key to reducing emissions to the atmosphere and standing against climate change. However, the risk of CO_2 leakage from geological reservoirs to other rock formations requires a careful long-term analysis of the system. Especially, oil well cement used for the operation must withstand the carbonation process that changes its poromechanical behavior over time, possibly affecting the system's integrity.

This work focuses on the microstructure and mechanical behavior of cement modified with bacterial nanocellulose (BNC) cured at 90 °C, simulating temperature at the reservoir level. The chemo-hydro-mechanical (CHM) coupled behavior of the cement-rock interface is also investigated through numerical analyses.

Mercury intrusion porosimetry (MIP), X-ray diffraction (XRD), ultrasonic wave measures, and unconfined compressive strength (UCS) tests were performed on cement samples subjected to a supercritical CO_2 environment. After carbonation, BNC samples show a lower mass gain and lower porosity compared to PC. Permeability based on MIP results indicates that the BNC reduces the permeability of the specimen. XRD quantification shows no substantial difference between the crystalline phases of the two samples. Samples with BNC have lower absolute strength but higher relative increase during carbonation.

The numerical study includes a homogenization of the medium considering the contribution of all components. CHM behavior of the cement with BNC is analyzed, and the results show the variations of the physical and chemical properties across the sample. The numerical study shows the advantage of using this type of tool for the study of realistic CO_2 injection scenarios in deep wells.

Keywords

CO_2 geological storage, cement paste, bacterial nanocellulose, reservoir temperature, chemo-hydro-mechanical couplings.

1. Introduction

There is an increasing rate of greenhouse gas emissions into the atmosphere. This can have consequences for different ecosystems and human health[1]. The carbon dioxide capture and storage (CCS) technology is an effective solution to reduce these emissions of CO_2[2]. This technology allows storing massive amounts of CO_2 underground in geological reservoirs[3,4]. It is important to know the storage capacity of the reservoir, but this highly depends on temperature and pressure. Reservoirs deep enough to store CO_2 in a supercritical state ($scCO_2$) present considerably higher capacities compared to shallower reservoirs with similar pore volume. Furthermore, high pressures and temperatures just above the supercritical point considerably increase the fluid density, and therefore the amount of CO_2 that can be stored[2]. Other key factors are the porosity and permeability of the reservoir rock. For instance, the “Sicily Channel” and “Abruzzi Offshore” reservoirs are candidates for geological storage, with porosities reaching 25.6% and permeability of 358 mD[5]. On the other hand, shale formations can also be considered for storage of CO_2, as indicated by studies on the SACROC Unit reservoir, since shale rock have porosities of around 10% and permeability of 10-100 mD, ensuring that their sealing capacity can be maintained for decades[6].

The caprock formation is an impermeable barrier that covers the upper part of the reservoir and prevents CO_2 leakage to other geological formations. However, during drilling, the zone near the well is damaged. Existing or drilling-induced faults/fractures in the caprock could turn into leakage paths of CO_2 to upper environments. An annular cement barrier is placed between the steel casing and the rock formation to maintain the wellbore integrity after the drilling fluids are removed.

Several problems arise in this system during CO_2 injection, two of which are temperature gradients[7] and induced seismic activity[8]. These effects change the stress states and can lead to failure of the cement or rock. Furthermore, cement Class G used in the oil industry is chemically unstable against

CO_2 and $scCO_2$[9]. Geochemical studies of cement paste show that the advance of carbonic acid through cement paste mainly induces the chemical reaction of portlandite (CH) and hydrated calcium silicates (C-S-H), and the precipitation of calcium carbonate (CC)[10]. These chemical reactions induce changes in porosity and the mineral composition of the solid phase. The first reaction of carbonation in cement is between CH and CO_2:

$$\mathrm{CH} + \mathrm{CO_2} \rightarrow \mathrm{CC} + \mathrm{H_2O} \text{ (Simplified)} \quad (1)$$

In absence of CH, the pH level is significantly reduced, allowing the second reaction that consists of the carbonation of the C-S-H:

$$0.625\ \mathrm{C-S-H} + \mathrm{CO_2} \rightarrow \mathrm{CC} + 1.3\ \mathrm{H_2O} + 0.625\ \mathrm{SiO_2(H_2O)_{0.5}} \text{ (Simplified)} \quad (2)$$

The formation of amorphous silica from C-S-H could increase porosity, depending on the C-S-H structure[11], and may reduce structural integrity. Furthermore, $CaCO_3$ precipitated in a water acidified medium in the presence of CO_2 is in turn prone to dissolution[12]. This dissolution continues until thermodynamic equilibrium is reached[13], increasing porosity, permeability, and reducing compressive strength[14]. The cement matrix, after complete carbonation and degradation, may result in a porous medium of low resistance, unable to maintain the integrity of the borehole or the ability to seal against external loads[15,16] .

The modification of cement to improve some properties is a subject of interest in the cement wellbore industry. The objective is to modify the cement matrix, making it lighter while maintaining high strength and low permeability in its hardened state. New additives such as nanocellulose are being added to the mix to improve the cement properties[17]. Nanocellulose can be used as a crack-inhibitor to avoid cement damage and thus prevent CO_2 leakage through the upper formations[18,19]. Bacterial nanocellulose (BNC) is a type of nanocellulose obtained from bacteria of the genus Gluconacetobacter. This material is produced by a partner company, and obtained in a more economical and less polluting way than other polymers[20]. Nanocellulose is considered as a potential additive to improve cement properties, such as mechanical and thermal resistance, and to decrease transport phenomena by reducing cement porosity[21–23]. In turn, its use can be extended in the oil industry in cementing operations.

The effect of bacterial nanocellulose (BNC) on the porosity and mechanical behavior of oil well cement paste cured at 20ºC and atmospheric pressure has been recently studied[22,24]. Barria et al.[22] show that BNC increases compressive strength and thermal stability in non-carbonated samples.

BNC-cement samples subjected to $scCO_2$ conditions show a density increase and a reduction in porosity, while the carbonation degree is reduced, therefore the mechanical behavior is less affected compared to non-modified cement[24]. Nevertheless, its behavior at different curing conditions like those in a reservoir is unknown.

Temperatures in the various geological reservoirs (coal beds, deep saline aquifers, or depleted oil and gas reservoirs) can vary depending on the depth at which they are found. In some reservoirs, the temperature can vary from 60 to 160 °C [25], being 90 °C a value usually used by other authors experimenting with cement[26–29].

This work focuses on the microstructure and mechanical changes of cement pastes with added bacterial nanocellulose and cured at 90 °C in the context of CO_2 reservoir conditions. Mercury intrusion porosimetry (MIP), X-ray diffraction (XRD), ultrasonic wave measurement, and unconfined compressive strength (UCS) tests were performed on BNC-cement samples subjected to supercritical CO_2 conditions to characterize its behavior. A finite-element-based numerical analysis of the chemo-hydro-mechanical (CHM) coupled behavior of the cement-rock interface accounting for the obtained experimental data is then carried out to explore realistic scenarios of CO_2 injection in deep wells.

2. Experimental program

Cement samples modified with bacterial nanocellulose were cured at 90 °C, simulating temperature at reservoir level prior to being carbonated under wet supercritical CO_2 conditions. Porosimetry and mechanical tests were performed on these samples to study the evolution of the microstructure and mechanical behavior.

2.1 Materials

The cement used in this study was Class G Portland Cement. The cement composition obtained by X-ray fluoresce is C_3S 52.8%, C_3A 1.6%, C_2S 21.1% and C_4AF 15.5%[22].

Bacterial nanocellulose (BNC) used is a biopolymer derived from the aerobic fermentation of bacteria of the genus *Gluconacetobacter*[30]. This biopolymer is a membrane with 98% of water and 2% of bacterial nanocellulose. The membrane is formed by micrometric fibers of nanometric thickness. Deionized water and a polycarboxylate ADVA 175 LN High-Performance Water-Reducing Admixture were used in the mixture.

2.2 Preparation of cement samples

Bacterial nanocellulose additive was prepared by grinding the BNC membranes and using ultrasound to generate a homogeneous fluid[22]. Cement mixtures were made following the American Petroleum Institute (API) Standard 10A[31] and pouring the slurry in cylindrical molds. They were cured in a 90 °C batch, unmolded after 24 hours, and kept underwater for 48 hours. They were then dried at 85 °C for 1 week[26], simulating a dry cure in the wellbore. A group of 16 samples; 8 non-modified cement (PC) and 8 with 0.05% of BNC (BNC05) were prepared and cored with a diamond wire saw into 76 mm long cylinders with a diameter of 38 mm each.

2.3 Carbonation

The accelerated carbonation under wet supercritical CO_2 conditions was carried out in a vessel of 4020 cm^3 of volume at 90 °C and 20 MPa for 30 days. The samples were placed on a container grid inside the cell. 500 ml of water were placed at the bottom of the vessel to maintain humidity. First, the vessel was pressurized with CO_2 until 8 MPa. Then, the temperature of the vessel was raised to 90 °C and the pressure was regulated until 20 MPa. These conditions were maintained during the entire test. Once the test finished, the heating system was turned off and the pressure was slowly released until atmospheric pressure. **Fig. 1** shows the equipment used. 4 Portland Cement (PC) samples and 4 modified cement samples with 0.05% BNC (BNC05) were carbonated for 30 days.

2.4 Porosimetry measurement and permeability estimation.

The pore size distributions of the BNC-cement samples were characterized by means of mercury intrusion porosimetry (MIP). The AutoPore IV 9500 Micromeritics with a maximum pressure of 230 MPa was used to measure pore sizes between 5 nm and 300 μm. Samples of approximately 1 cm^3 were taken from a representative zone of the non-carbonated cement samples and, in the case of the carbonated cement, samples were taken from the core and the most degraded zone near the exposed surface. Before testing, samples were dried by the freeze-drying method.

The effect of curing the samples in the oven (Section 2.2) for 1 week was measured. For this purpose, air-cured samples (PC-Reference) and oven-cured samples (PC-NC and BNC05-NC) were compared. NC means non-carbonated samples, while 30INT and 30EXT are 30-days carbonated samples located at the interior and exterior of the bulk sample, respectively. The tests performed are listed in **Table 1**.

By assuming cylindrical interconnected pores, we can calculate the pore diameter corresponding to each mercury pressure step by:

$$p = \frac{4\gamma \cos(\theta)}{d} \quad (3)$$

where γ = mercury surface tension = 0.485 N/m, θ = mercury contact angle = 130°[32], p = mercury pressure, d = pore diameter.

An estimate of permeability can be made from the results obtained in the MIP test. This estimation is performed by considering the macro-scale flow with Darcy's law and the micro-scale flow with Poiseuille's law.

Each pore of class i of diameter d_i has an intrusion volume of mercury V_i, so a length L_i can be determined for each pore class i:

$$L_i = \frac{4\,V_i}{\pi d_i^2} \quad (4)$$

Assuming laminar flow, the Poiseuille's flow in a cylindrical tube depends on the difference of pressures at the tube ends, the dimensions of the tube, and the viscosity of the fluid. So the flow for each tube of diameter d_i is:

$$Q_{Poiseuille} = \frac{\Delta V}{\Delta t} = \frac{\Delta P_i\,(\pi\, d_i^4)}{128\, L_i\, \eta} \quad (5)$$

Where ΔP_i is every mercury pressure step and η is the dynamic viscosity of the fluid.

Once the total flow rate is obtained, Darcy's law can be used to determine the permeability at the macro-scale. Let V_t be the total apparent volume of the MIP sample (ratio of total pore volume to porosity). The average pore length L_e is defined as:

$$L_e = \sqrt[3]{V_t} \quad (6)$$

The hydraulic gradient i is given by:

$$i = \frac{\Delta P_t}{Le} \quad (7)$$

Where ΔP_t is the total pressure increase in meters' water column measured in the MIP.

Therefore, the intrinsic permeability of the material (independent of fluid conditions) is:

$$\kappa = \frac{\sum_1^n Q_{Poiseuille}}{S\,i} \left(\frac{\eta}{\rho_f\, g}\right) \quad (8)$$

Where n is the total number of pores of different diameters, S is the cross-section of a cubic specimen with sides of length L_e, ρ_f is the density of the fluid and g is the gravity.

The calculated permeability accounts for an isotropic flux in a cubic sample. Hence, it needs to be divided by three to compare with the directional permeability obtained experimentally. This indicates that the fluid flows equally in the three directions of space [33].

The specimens analyzed to calculate permeability were carbonated and non-carbonated samples of both types of cement (PC-NC, PC-30EXT, BNC05-NC, BNC05-30EXT).

2.5 X-ray diffraction (XRD)

X-ray diffractograms were obtained in a Philips 3020 diffractometer using CuKα radiation with a Ni-filter (35 kV, 40 mA). Scanning was performed between 3° and 70° 2θ, with a step of 0.04° and a count time of 2 s/step. The openings of the divergence, reception, and dispersion slots were 1, 0.2 and 1° respectively, and no monochromator was used. The identification of the mineral phases in the material was performed using the X'Pert High Score program. The standard procedures described in the literature and described by Moore and Reynolds[34] were followed for the identification and quantification of the minerals. Quantification was based on the work of Biscaye[35].

2.6 Ultrasonic wave measurement

The equipment used was a portable EPOCH TX ultrasonic with P and S ultrasonic waves measurements. Two transducers were placed on the top and bottom surfaces with a thin layer of gel to ensure full contact between the specimen surfaces and the transducers. The time it takes for the P and S elastic wave signals to travel through the sample was measured and divided by the length of the sample. The shear and bulk moduli are then calculated by:

$$G = \rho V_s^2 \text{ and } K = \rho\left(V_p^2 - \frac{4}{3}V_s^2\right) \quad (9)$$

While the Young's Modulus and Poisson coefficient are calculated by:

$$E = \frac{9KG}{3K+G} \text{ and } \nu = \frac{3K-2G}{6K+2G} \quad (10)$$

2.7 Mechanical testing

The uniaxial compression tests were performed on a 100 kN universal testing machine by imposing a velocity rate of 0.5 mm/min. The carbonated and non-carbonated mixtures were tested. The average strength value was calculated from 3 tested cylindrical samples of 38 mm in diameter by 76 mm height. Maximum compression strength and Young's modulus were obtained for all samples.

3. Chemo-mechanical analysis of carbonated samples

The experimental study has been complemented with the analysis of the chemo-poro-mechanical coupled behavior of the cement with added 0.05% BNC and reacting with the CO_2. The model simulates the carbonation front advance in cement subjected to $scCO_2$ and the changes generated by the chemical reactions by using the classic balance equations of continuum mechanics relative

to mass, momentum, entropy, and energy[36,37]. It is assumed that the porous solid remains saturated by the fluid (i.e. $scCO_2$ does not penetrate within the pores of the cement)[38,39]. CO_2 is present in the skeleton as a dissolved species within the fluid.

When cement is carbonated, porosity undergoes several variations. Some are due to chemical reactions, denoted ϕ_L for leaching of cement matrix and ϕ_P for calcite precipitation. The other variations of porosity are due to the deformation of the porous medium, with φ_F and φ_C as the deformation of the porosity filled by fluid phase and by calcite phase, respectively. The porosities involved can be written as follows:

$$\phi_F = \phi_0 + \phi_L - \phi_P + \varphi_F \tag{11}$$

$$\delta_C = \phi_P + \varphi_C \tag{12}$$

Where ϕ_F corresponds to the pore volume occupied by the in-pore fluid per unit of initial volume of the porous medium, ϕ_0 corresponds to the initial pore space per unit of initial volume of porous medium which is not occupied by the solid phase. The difference between these two porosities is denoted by δ_C, which is the pore volume occupied by carbonate crystals[36].

The constitutive equations of isotropic linear poroelastic material of an infinitesimal representative volume element of a porous medium ($d\Omega_0$) are derived from Gibbs-Duhem equalities and Clausius-Duhem inequality assuming isothermal conditions:

$$\boldsymbol{\sigma} - \boldsymbol{\sigma_0} = \left(\mathrm{K} - \frac{2}{3}\mathrm{G}\right)(\varepsilon - \varepsilon_0)\mathbf{1} + 2\mathrm{G}(\boldsymbol{\varepsilon} - \boldsymbol{\varepsilon_0}) - \sum_{\mathrm{k=F,C}} \mathrm{b_k}\left(\mathrm{p_k} - \mathrm{p_{k,0}}\right)\mathbf{1} \tag{13}$$

$$\varphi_J - \varphi_{J,0} = b_J(\varepsilon - \varepsilon_0) + \sum_{k=F,C} \frac{p_k - p_{k,0}}{N_{JK}}; J = F, C \tag{14}$$

where $\boldsymbol{\sigma}$ and $\boldsymbol{\varepsilon}$ are the stress tensor and infinitesimal strain tensor, $\varepsilon = \mathrm{tr}(\boldsymbol{\varepsilon})$ is the volumetric strain, K and G are the bulk modulus and shear modulus in drained conditions, respectively. φ_J is the deformation of the porous volume occupied by the phase *J (F* stands for fluid and *C* for carbonates*)*, while b_J and N_{JK} are the generalized Biot coefficients and the generalized poroelastic coupling moduli[40].

The coupling with the chemical reactions taking place during carbonation is established from the mass conservation law of the fluid and CO_2. Equation 15 is the fluid mass conservation, while Equation 16 is the conservation of the molar amount of CO_2:

$$\left(\frac{\rho_f \phi_f}{K_f} + \frac{\rho_f}{N_{FF}}\right)\frac{\partial p_f}{\partial t} + \rho_f b\, div\left(\frac{\partial \boldsymbol{u}}{\partial t}\right) + \rho_f \sum_{R_i} Y_{Ri} \frac{\partial \xi_{Ri}}{\partial t} - div\left(\rho_f \frac{\kappa}{\eta} grad\, \rho_f\right) = 0 \tag{15}$$

$$\frac{\partial(\phi_f\, c_{CO_2})}{\partial t} + \sum_{R_i} a_{Ri} \frac{\partial \xi_{Ri}}{\partial t} - div\left(d_{eff}\,\boldsymbol{grad}\, c_{CO_2} + c_{CO_2} \frac{\kappa}{\eta}\boldsymbol{grad}\,\rho_f\right) = 0 \quad (16)$$

where ρ_f, ϕ_f, K_f, p_f are the density, porosity, bulk modulus, and pressure of the fluid. a_{Ri} is the stoichiometric coefficient of the reaction Ri, c_{CO_2} is the CO_2 concentration in fluid, η is the dynamic viscosity of the fluid phase, Y_{Ri} is a variable that depends on the molar volumes of reactive species, $\boldsymbol{u}$ is the skeleton displacement vector, ξ_{Ri} is the reaction advance depending on κ and d_{eff}, which are the permeability and diffusion coefficients.

The progress of carbonation is governed by the parameters of CO_2 diffusion in the fluid and by advection:

$$\frac{\partial \xi_{Ri}}{\partial t} = div\left(d_{eff}\,\boldsymbol{grad}\,\frac{n_{CO_2}}{\phi_f} + n_{CO_2}\frac{\kappa}{\eta}\boldsymbol{grad}\,\rho_f\right) \quad (17)$$

where n_{CO_2} corresponds to the apparent CO_2 concentration. It should be noted that C-S-H carbonation does not start until the portlandite is completely carbonated, since Portlandite maintains a high pH level (pH > 12).

Since cement is a heterogeneous multiphase material, a homogenization technique was used to replace the heterogeneous media with a homogeneous media that behaves in the same manner[41]. A modification in the homogenization formulation has been introduced to account for the contribution of bacterial nanocellulose (BNC) characteristics to the overall characteristics of modified Portland class G cement. The model is implemented in the finite element code BIL 2.3.0[42].

Chemical reactions (carbonation-dissolution) occurring in the system induce changes in the transport and mechanical properties of the system. The main parameters that influence the carbonation advance are the intrinsic permeability κ and the diffusion coefficient d_{eff}. Advection behavior is subjected to the medium permeability and fluid flux, while diffusion is ruled by Fick's Law. Both phenomena are in turn intimately linked to the initial cement porosity[43,44]. For this type of cement, it can be evaluated using:

$$\kappa = \kappa_0 \left(\frac{\phi_F}{0.26}\right)^{11} 10^{-19}\ \mathrm{m}^2 \quad (18)$$

where κ_0 is a parameter to calibrate.

The variation of the porosity must be taken into account in the expression of the effective diffusion coefficient considering a porous medium. The effective diffusion coefficient is ϕD, while D is the

diffusion coefficient of the solute in the interstitial pore solution. Based on experimental data, Mainguy and Coussy[45] propose the following expression for the effective coefficient of diffusion:

$$d_{eff} = d_{eff,0}\, e^{(9.95\phi_F - 29.08)} \quad (19)$$

Being $d_{eff,0}$ a parameter to calibrate.

These equations are empirical and aimed at reasonably representing the transport phenomena occurring within the cement matrix. Parameters κ_0 and $d_{eff,0}$ can be modified to obtain values of intrinsic permeability and diffusivity suitable for class G or H cement.

4. Experimental results and discussion

Fig. 2 shows the longitudinal cut of samples after 30 days of carbonation. Brown color represents the most degraded part of cement due to carbonation, the color probably being due to iron hydroxide released from chemical reactions[6]. PC samples show a more intact core compared to BNC05.

The penetration depth had important progress on the cement cured at 90 °C after 30 days of carbonation. These results are similar to values obtained by other authors for curing and carbonating under similar conditions[26,46]. There are some uncertainties based on studies by previous authors, mainly from the curing conditions before carbonation. Indeed, water to cement ratio, curing temperature, pressure, and duration will change the carbonation results, so different curing conditions and equal carbonation procedures will yield different results. Some previous experiences have short curing times for the cement[26,46], and show high CO_2 penetration, while some other authors performed longer curing periods[47,48], showing less penetration. Recent works have shown that cement with lower density allows a higher CO_2 penetration[49]. Furthermore, a higher hydration degree is tied with density increase, and porosity reduction[50], thus maintaining a high temperature during a short curing period will allow deeper CO_2 penetration into the cement samples and more advanced chemical reactions.

In this work, carbonation led to an increase in the density of PC and BNC05 samples. Before carbonation, a slight difference is noted between PC and BNC05 samples, with densities of 1.89 and 1.87 g/cm^3, respectively. Once the samples were carbonated, density increased until 2.13 and 2.11 g/cm^3 for PC and BNC05 (**Table 2**). PC shows an average mass uptake of 13.2% while BNC05 shows an average of 12.9%, meaning that fewer chemical reactions have taken place. The mass gain is similar to previous works under similar conditions[46], however, the penetration depth is different. Our results are closer to the penetrations observed by Fabbri and co-workers[26], even

296 though our samples are not fully carbonated after 30 days. This is because our samples are larger,
297 therefore more chemical CO_2-bonds are needed to carbonate more volume and chemical reactions
298 are limited by diffusion of CO_2.
299 The oven-drying conditioning for one week at 85 °C has not significantly affected the MIP porosity
300 or the pore size distribution from non-conditioned samples (**Fig. 3**). MIP porosity performed on these
301 samples increased for both cement types from 33.7% to 34.5%, prior to the carbonation test, and
302 the characteristic peak is approximately 50 nm. Samples with bacterial nanocellulose did not
303 significantly modify the cement in terms of porosity or pore size distribution compared to PC cement
304 cured at 90 °C. It is likely that bacterial nanocellulose is not having the same effect in inhibiting the
305 larger cracks produced by the high curing temperature.
306 Calorimetry tests have shown that BNC initially acts as a cement retarder[51,52]. As the curing time in
307 this work is short, the porosity of BNC-cement is similar to PC with some coarser pores at 0.2 μm.
308 Nevertheless, for longer curing periods, for instance, cement cured at 20 °C for 28 days, cement
309 structure is denser and more compact, so in these conditions, bacterial nanocellulose is more likely
310 to develop a fiber network inside the cement and to increment hydration degree[53,54], as it tends to
311 release adsorbed water which contributes hydration[18].
312 The MIP results after the carbonation of PC are presented in **Fig. 4**. Here we can observe that the
313 porosity variation along the radial direction leads to smaller pores and to smaller porosity values,
314 while the characteristic peak is shifted to pores smaller than 10 nm. After carbonation, no major
315 change is observed due to the addition of BNC. Porosity decreased to 24.5% at the core and to
316 21.5% near the exposed surface. BNC05 shows similar results to PC (**Fig. 5**), and its porosity
317 decreased at the core to 23.2% and near the exposed surface to 21%. The slight mass uptake is
318 due to the consumption of CO_2 by the occurring chemical reactions and is reflected by these small
319 porosity variations. Reduced porosities lead to less diffusion of CO2 into the cement core and
320 therefore increase the time to reach full carbonation of the samples.
321 The permeability results in **Table 3** are consistent with the intrinsic permeability values of cement
322 cured at a high temperature. This method simplifies the complexity of crosslinking between different
323 cylinders of different pore diameters and considers a tortuosity of 1 [55]. The Li values are very high
324 for small diameter pores, so a higher deviation error is also induced.

In this analysis, cement with nanocellulose addition appears to have lower permeability than cement without additions. After carbonation, the permeability values of PC are reduced by one order of magnitude, while the permeability in cement with BNC addition is in the same order of magnitude as the initial value. Experiments on carbonate cement samples are necessary to validate these results.

Fig. 6 presents the XRD patterns of the samples before and after carbonation. The relative percentages of the crystalline phases are presented in **Table 4**. The analyses show the contents of portlandite, katoite, brownmillerite, magnesite, aragonite, and calcite.

Portlandite is one of the main cement hydration products with high crystallinity, while C-S-H is a low crystallinity amorphous material. Brownmillerite is a phase of Clinker denominated as C_4AF. Aragonite and calcite are calcium carbonates of a different crystalline system with Orthorhombic and Rhombohedral shapes, respectively. When the study temperature is high, new crystalline phases such as katoite appear. Katoite is a calcium aluminate hydrate more stable at high temperatures than ettringite.

The results of **Table 4** in cement without supercritical carbonation indicate approximately 60% hydrated material (portlandite and katoite), 25% carbonated material (calcite and magnesite), and 15% non-hydrated and non-carbonated material (browmillerite). It can be determined that during the curing process prior to supercritical carbonation, 25% of crystalline material is already carbonated. The lack of crystals related to C-S-H is due to the insufficient intensity of reflection of this amorphous material [56]. It is possible that the short curing time has generated a low reflection tobermorite and that the small readings have been incorporated into the crystalline phase of the katoite or calcite.

After supercritical carbonation, the most affected materials were portlandite and katoite as the XRD shows no cement hydration materials, indicating complete carbonation. Magnesite also seems to have been consumed, allowing more calcium carbonates to be created. Approximately 93% are carbonate crystalline materials, the remaining 7% is C_4AF from the clinker phase that did not chemically react.

The results of the PC and BNC05 samples before and after carbonation are similar to each other, suggesting that the BNC did not have a significant effect on the microcrystalline structure of the cement under these curing conditions.

Table 5 shows the mechanical properties measured by V_S and V_P. Overall, during the carbonation process, mechanical properties increase. This is corroborated by UCS tests. The samples show an increment in compressive strength and also in their Young's modulus (**Fig. 7**). PC strength initially was 31 MPa and after the carbonation stage, it increased by 44%, while BNC05 started with 24 MPa of strength, which increased by 60% with carbonation. Both types of cement initially had Young's modulus of 20 GPa, unlike the 25 GPa in long-cured specimens[24], but after carbonation, this modulus increased by 11% for PC and by 18% for BNC05.

Nanocellulose has been reported to improve the mechanical properties of cement composites for well-hydrated cement[19,57,58]. In the present work, BNC05 samples initially have compressive strength lower than PC samples and comparable Young moduli. These observations distinguish from the results previously obtained with cement cured at room temperature over a long period[22]. Curing at a higher temperature is probably generating larger cracks in the cement, so the microstructural effect of BNC does not substantially improve the mechanical behavior. Or this effect appears later because of the retarder effect of BNC or the superplasticizer, which slow down the hydration rate of the modified cement, and thus the hydration degree at the end of the curing time.

It is well known that carbonation under atmospheric conditions tends to increase the mechanical properties of cement[59,60]. However, there is no agreement on cement strength variations after supercritical carbonation[46]. In supercritical conditions, some results show an increment in compressive strength[61,62], while more recent researchers were able to see a decrease in mechanical performance[26,63,64]. This variation is due to different conditions of cement hydration prior to carbonation [65] and subsequent carbonation conditions[62]. Indeed, experiments using the same cement and water to cement ratio and same carbonation conditions show a drop in strength values[24]. After short curing conditions, during carbonation, cement will not be fully hydrated, and the mechanical performance increment after carbonation will be most likely due to the cement matrix development by hydration acceleration imposed by temperature in the carbonation cell. The mechanical properties of the tested material will be a combination of the effects of cement hydration compounds and precipitated calcite that has been produced during carbonation. On the other hand, well-hydrated cement will only experience a drop in strength due to C-S-H degradation and porosity increase over time[24,48,64,66]. In this work, supercritical carbonation is positively affecting the mechanical performance of cement. These observations are intricately linked to the carbonations

conditions. Indeed, if cement carbonation is imposed by a continuously renewed fluid flushing, then the products of carbonation (mainly carbonates), will in turn dissolve and be flushed out, leading to a strong increase in porosity of the cement, and degraded mechanical properties. In the present experiment, CO_2 penetrates the sample by dissolution and diffusion in the pore fluid, which is not renewed.

Since CC has better mechanical performance than CH, CC precipitation should increase mechanical performance and Young's modulus. This effect can take place here because of the continuous hydration of cement inside the reactor, which is linking the precipitated CC with the cement matrix. These two effects are increasing mechanical properties as seen by Fabbri et al. and Sauki et al.[26,62], but cement hydration plays the most significant role during the carbonation process. This can also be observed from V_P and V_S wave data, where mechanical parameters increased. However, Young's moduli differ from the ones measured by UCS tests. Young's moduli measured by elastic waves are 19.5 and 21.3 GPa for PC before and after carbonation, while for BNC05, it measured 18 and 20,5 GPa. The real values obtained from UCS tests showed 20 GPa for both cement before carbonation, while after carbonation, it showed 22.2 GPa and 23.6 GPa for PC and BNC05, respectively.

After carbonation, **Fig. 7** shows that the increase in the relative strength and Young modulus of BNC05 is greater compared to PC. This is linked with cement hydration during carbonation, where the hydration kinetics have been enhanced in BNC-samples by the hydrophilic properties of the bacterial nanocellulose[54] and its ability to release water during hydration[18].

5. Numerical analysis of carbonated samples

In this section, the numerical analysis of the carbonated BNC samples is presented. A 2D analysis is performed simulating the experimental carbonation of the cylindrical samples. Calibration on the model is made by taking the porosity values obtained experimentally to estimate the intrinsic parameters of this cement. The initial volumetric proportions of the minerals in the cement are estimated from the literature. The calibrated model is extrapolated to simulate in 1D the cement carbonation in a wellbore system under downhole conditions.

5.1 Initial parameters and intrinsic properties of cement

Porosity is very variable for cement and depends mainly on the water to cement ratio and on the type of curing in which the specimen is placed. Some authors estimate porosities greater than 30%[28,46,67,68], while others approximate it from 20% to 30%[69–72]. Regardless of the kind of oil cement

414 in question (G or H), it can be generalized that the porosities of oil cement are around 25% to 35%.
415 The initial porosity of the samples in this work before carbonation is 34.5% as indicated in Section
416 4.
417 The volumetric content of cement minerals depends substantially on the cement type, water to
418 cement ratio, hydration degree, and curing temperature. So, it is necessary to estimate these
419 proportions for the simulation. In some articles, the amount of Portlandite CH varies between 15 to
420 25%[43,70], with commonly accepted values being percentages of 18 to 20%[36]. In previous results,
421 using the same cement and same water to cement ratio[22], a percentage of 20% was obtained by
422 thermogravimetric analysis on well-hydrated cement samples. Class G and H cement have very low
423 initial aluminate contents following API requirements aiming at being resistant to sulfate attacks
424 (C3A ≤ 3% and C4AF + 2 C3A ≤ 24%). So the hydrated aluminate components have a low
425 percentage, around 6 to 14%[36,69,73]. Finally, the most important phase of cement in terms of
426 compressive strength, C-S-H, can vary between 60 to 27% in volume fraction[36,73].
427 The intrinsic permeability is independent of the conditions to which the material is initially subjected,
428 at least directly. Since cement is a heterogeneous material, there is no unique intrinsic permeability
429 value for cement. Nelson et al.[61] in their experiments report values of $1x10^{-16}$ m^2 to $1x10^{-20}$ m^2. This
430 is supported by Ghabezloo et al.[70] and Mainguy et al.[74], who obtain values in the order of $1x10^{-19}$ m^2
431 y $1x10^{-20}$ m^2. Sercombe et al.[72] show values of $1x10^{-16}$ m^2 after excessive heating on hardened
432 cement paste, so it can be assumed that this order of magnitude refers to cracked cement.
433 The diffusivity of cement for class G and H has also been variable, as reported by different authors.
434 Huet et al.[75] performs a compilation of the different transport mechanisms of cement G subjected to
435 an environment of $scCO_2$ and quotes diffusivity values of $1x10^{-12}$ m^2s^{-1} down to $1x10^{-14}$ m^2s^{-1}.
436 Mainguy et al.[74] give an example of diffusion in the order of $1x10^{-12}$ m^2s^{-1}, and Vallin et al.[36] determine
437 a value of $1x10^{-10}$ m^2s^{-1} on the simulation. Furthermore, Shen[76] quotes the values of different
438 aqueous species in the order of $1x10^{-9}$ m^2s^{-1}.
439 To obtain the diffusion and permeability parameters for this particular cement for later use in the
440 simulation at reservoir level, a porosity value equal to the experimental value of 34.5% for the first
441 simulation is considered. As the rest of the volumetric proportions are variable, values were adopted
442 from literature considering a 0.05% content of BNC: C-S-H 40.5%, CH 18%, aluminates 6.942%,
443 and BNC 0.058%. The remaining compounds are classified as inert components, including

amorphous silica which is a carbonation product. CO_2 concentration is calculated considering: water volume, temperature, pressures, and mole fraction of CO_2 from experiments. The calculations give values of 1200 mol/m^3.

The initial parameters for fluid and cement are listed in **Table 6**, where η_{vis} is the fluid viscosity, K_F the fluid compressibility, ρ_F is the fluid density, R_c is cement compressive strength, and R_t the tensile strength. **Table 7** shows the molar volumes of the compounds involved.

The 2D model for the experimental carbonation consists of one-quarter of a sample (19 mm-radius by 38 mm-height) using a mesh of 22x11 elements (**Fig. 8**). The lower horizontal contour has restricted movements in the X direction, while the left vertical contour has restricted movements in the Y direction. The top and right-hand contours are subjected to the carbonation conditions. **Table 8** shows the initial conditions for modeling.

The well-system modeled consists of a CO_2 reservoir drilled and refilled with a steel casing protected by an annular cement geometry. We used the same transport values after determining the advection and diffusion parameters from the previous simulation. The model for the wellbore simulation assumes 1D axial symmetry under plane strain conditions in the axial direction. The mesh of ¾ of an inch (19 mm) represents the annular cement thickness and allows studying the progress of carbonation from the outer surface towards the inner cement. It consists of 502 elements that have the properties of the modified cement with BNC. Previous conditions for temperature and fluid pressure are considered (that is 90 °C and 20 MPa) with a 1.2 CO_2 molarity.

5.2 Results and discussion

First, a sensitivity analysis of parameters to calibrate the numerical model is made to reproduce the experimental penetration results. **Table 9** and **Table 10** show the values of the intrinsic permeability and diffusion coefficient varying κ_0 and $d_{eff,0}$. As it can be observed, the values of permeability and diffusivity are in the range of the admissible values for cement class G previously mentioned.

By calibrating the model for κ_0=350 and $d_{eff,0}$=160, a representation of the entire sample consistent with the MIP experimental results of porosity can be observed in **Fig. 9**. Results clearly show how the carbonation advanced into the core. The 1D image shows the porosity variation as a function of the radius. The material near the exposed surface is completely carbonated, and the porosity reaches 21%, while at the core, the porosity average is similar to the 23,2% from the MIP experiments.

Fig. 10 shows in more detail the dissolution and carbonation fronts. The blue line corresponds to the starting point of the chemical reaction of CH, while the red line is the limit between the carbonation process and where the hydrated products have already been carbonated. Some authors consider that the carbonation front or penetration depth follows a linear trend as a function of the square root of time (consistently with the fact that the chemical reactions are limited by the diffusion of CO_2 within the fluid phase)[77,78]. Nevertheless, this is usually based on the phenolphthalein test which only considers the pH below 9. With the present model, we can distinguish the two fronts. In a first contact between the cement and $scCO_2$, there is a significant decrease in CH and C-S-H content that lasts for the first few days. After 10 days, the dissolution front reaches the center of the cement sample. The complete reaction of CH and C-S-H front advances almost linearly in time but, it does not reach the cement center. Calcite is mostly deposited in the material near the exposed surface, decreasing its porosity, while in the core, it has not yet completely precipitated.

Even though the dissolution front has reached the center, the chemical reactions between CO_2 and CH/C-S-H, which produce CC and water are still taking place in a region located 1 cm away from the center, meaning that all CH and C-S-H have not yet been completely leached after 30 days in these conditions.

The calibrated parameters are extrapolated to the cement submitted under downhole conditions in the context of CO_2 geological storage. We have to keep in mind that in the experimental results, curing and carbonation conditions are unfavorable to cement. However, the numerical can be adapted to any condition considered. From this approach, additional characteristics of the variability of the carbonation front using these transport parameters can be obtained: permeability (**Fig. 11**) and volumetric proportions (**Fig. 12**) variations throughout the sample. Carbonation advance forms calcite from CH and C-S-H, which grows inside the pores, this produces a reduction of the porosity and, as a consequence, a decrease in permeability and diffusivity, that slow down the entry of more CO_2 to the cement core. In **Fig. 11**, this can be seen as a clogging effect. After 5 days of carbonation, we can observe a considerable CO_2 penetration, but after 5 more days, the penetration rate has significantly slowed down. The penetration of calcite in **Fig. 12** starts with the CH area dissolution and continues with the C-S-H decalcification when there is no longer CH to consume. C-S-H decalcification continues creating CC and amorphous silica, which becomes part of the inert components.

6. Conclusion

The microstructure and mechanical changes of cement paste with bacterial nanocellulose additions and cured at 90 °C in the context of reservoir conditions were analyzed. Mercury intrusion porosimetry (MIP), X-ray diffraction (XRD), ultrasonic wave measurements, and unconfined compressive strength (UCS) tests were performed on BNC-cement samples subjected to supercritical CO_2 conditions to determine its behavior. In addition, a finite-element based numerical analysis of the cement-rock interface was presented.

BNC samples show a lower mass gain compared to PC, suggesting that fewer chemical reactions occurred. Nevertheless, the longitudinal sections of the BNC-cement present some small voids in their interior, which could allow further CO_2 penetration.

The MIP results show that initially, the samples with BNC have the same porosity as the cement without BNC addition. After carbonation, lower porosity is observed in cement with BNC, either in the core or near the exposed surface. From the MIP curves, a permeability analysis was performed. In this analysis, the samples with BNC show lower intrinsic permeability values than the cement without BNC.

The XRD results of the PC and BNC05 samples before and after carbonation show no difference from each other. After carbonation, the dominant crystalline phases are calcite and aragonite, which indicates the complete carbonation of the material.

Unmodified samples show a better mechanical performance during carbonation. However, carbonation in samples with BNC indicates a higher increase in relative strength than in samples without additions due to the BNC effect of releasing water during hydration inside the carbonation cell.

A chemo-poro-mechanical model of $scCO_2$ attack on a cement annulus of an abandoned oil well in the context of CO_2 storage was presented. A modification on the formulation was implemented to add the nanocellulose characteristics. The experimental data and simulation results were back analyzed to determine the properties of the cement used. Once these properties were known, a simulation under downhole conditions in the context of CO_2 geological storage was represented.

Results show a decrease in permeability and hydration products over time and the advance of the dissolution and carbonation fronts. The numerical study shows the advantage of the use of this type

of tool for the study of possible real scenarios of CO_2 injection processes in deep wells. It can be adapted to different systems under different established conditions.

Acknowledgments

The first author gratefully acknowledges the fellowship granted by the National Scientific and Technical Research Council of Argentina (CONICET) and to the EIFFEL fellowship program of Excellence granted by the Ministère de l'Europe et des Affaires étrangères of France. The authors acknowledged the financial support of the European Commission -H2020 MSCA-RISE 2020 Project DISCO2-STORE, Grant Agreement Nº 101007851-, the Universidad Nacional de la Patagonia San Juan Bosco -Project UNPSJB PI1614 80020190200006 IP, Res. R/9Nº207-2020 CRD1365 FI004/ 17-, the Agency of Scientific and Technological Promotion from the Argentine Republic. (Projects PICT 2016–4543, PICT 0843 2016), and the Institutional project ITPN PUE 0034 (CONICET). The authors also thank Dr. Siavash Ghabezloo and Dr. Teresa Piqué for helpful discussions, and also the technical staff of Petroquímica Comodoro Rivadavia and Laboratoire Navier for helping with the tests performed.

Nomenclature

γ:	*Mercury surface tension*
δ_C:	*Pore volume occupied by carbonate crystals*
ΔP_i:	*Mercury pressure step*
ΔP_t:	*Total pressure increase in meters' water column measured in the MIP*
$\boldsymbol{\varepsilon}$:	*Infinitesimal strain tensor*
ε:	*Volumetric strain. (*$\mathrm{tr}(\boldsymbol{\varepsilon})$*)*
η:	*Dynamic viscosity of the fluid phase*
θ:	*Mercury contact angle*
κ:	*Intrinsic permeability*
ν:	*Poisson's ratio*
ξ_{Ri}:	*Reaction advance*
ρ:	*Bulk density of the specimen*
ρ_f:	*Fluid density*
$\boldsymbol{\sigma}$:	*Stress tensor*
φ_C:	*Deformation of the porous medium filled by calcite phase*
φ_F:	*Deformation of the porous medium filled by fluid phase*
φ_J:	*Deformation of the porous volume occupied by the phase J*
ϕ_0:	*Pore space per unit of initial volume of porous medium not occupied by the solid phase*
ϕ_f:	*Fluid porosity*

567 ϕ_F: *Pore volume occupied by the in-pore fluid per unit volume of porous medium*
568 ϕ_L: *Porosity due to leaching of cement matrix*
569 ϕ_P: *Porosity due to of calcite precipitation*
570 a_{Ri}: *Stoichiometric coefficient of the reaction Ri*
571 b_J: *Generalized Biot coefficient*
572 c_{CO_2}: *Is the CO_2 concentration in fluid*
573 d_i: *Pore diameter*
574 d_{eff}: *Diffusion coefficient*
575 *i:* *Hydraulic gradient*
576 L_i: *Cylinder length of diameter i*
577 L_e: *Average pore length*
578 n: *Total number of pores of different diameters*
579 n_{CO_2}: *Apparent CO_2 concentration*
580 *p:* *Mercury pressure*
581 p_f: *Fluid pressure*
582 $\boldsymbol{u}$: *Skeleton displacement vector*
583 *E:* *Young's Modulus*
584 *G:* *Shear Modulus*
585 *K:* *Bulk modulus*
586 K_f: *Fluid bulk modulus*
587 N_{JK}: *Generalized poroelastic coupling moduli*
588 *S:* *cross-section of a cubic specimen with sides of length L_e*
589 V_i: *Volume of mercury intrusion into the pore of diameter i*
590 V_s: *Elastic S-wave velocity*
591 V_t: *Total apparent volume of the MIP sample*
592 V_P: *Elastic P-wave velocity*
593 Y_{Ri}: *Variable that depends of the molar volumes of reactive species*
594

595 ## References

596 1. Afroz R, Hassan MN, Ibrahim NA. Review of air pollution and health impacts
597 in Malaysia. *Environ Res*. 2003;92(2):71-77. doi:10.1016/S0013-
598 9351(02)00059-2

599 2. Philip Ringrose. *How to Store CO2 Underground: Insights from Early-Mover*
600 *CCS Projects*. Springer; 2020.

3. Michael K, Golab A, Shulakova V, et al. Geological storage of CO 2 in saline aquifers — A review of the experience from existing storage operations. *Int J Greenh Gas Control*. 2010;4(4):659-667. doi:10.1016/j.ijggc.2009.12.011

4. Bachu S, Bonijoly D, Bradshaw J, et al. CO2 storage capacity estimation: Methodology and gaps. *Int J Greenh Gas Control*. 2007;1(4):430-443. doi:10.1016/S1750-5836(07)00086-2

5. Civile D, Zecchin M, Forlin E, et al. CO2 geological storage in the Italian carbonate successions. *Int J Greenh Gas Control*. 2013;19:101-116. doi:10.1016/j.ijggc.2013.08.010

6. Carey JW, Wigand M, Chipera SJ, et al. Analysis and performance of oil well cement with 30 years of CO2 exposure from the SACROC Unit, West Texas, USA. *Int J Greenh Gas Control*. 2007;1(1):75-85. doi:10.1016/S1750-5836(06)00004-1

7. Vilarrasa V, Laloui L. Potential fracture propagation into the caprock induced by cold CO2 injection in normal faulting stress regimes. *Geomech Energy Environ*. 2015;2:22-31. doi:10.1016/j.gete.2015.05.001

8. Urpi L, Rinaldi A, Rutqvist J, Cappa F, Spiers CJ. Dynamic simulation of CO2-injection-induced fault rupture with slip-rate dependent friction coefficient. *Geomech Energy Environ*. 2016;7:47-65. doi:10.1016/j.gete.2016.04.003

9. Mason HE, Frane WL Du, Walsh SDC, Dai Z, Charnvanichborikarn S, Carroll SA. Chemical and Mechanical Properties of Wellbore Cement Altered by CO 2 - Rich Brine Using a Multianalytical Approach. *Environ Sci*

Technol. 2013;47:1745-1752. doi:dx.doi.org/10.1021/es3039906

10. Fernández Bertos M, Simons SJR, Hills CD, Carey PJ. A review of accelerated carbonation technology in the treatment of cement-based materials and sequestration of CO2. *J Hazard Mater*. 2004;112(3):193-205. doi:10.1016/j.jhazmat.2004.04.019

11. Shah V, Scrivener K, Bhattacharjee B, Bishnoi S. Changes in microstructure characteristics of cement paste on carbonation. *Cem Concr Res*. 2018;109(April):184-197. doi:10.1016/j.cemconres.2018.04.016

12. Matteo EN, Huet B, Jové-Colón CF, Scherer GW. Experimental and modeling study of calcium carbonate precipitation and its effects on the degradation of oil well cement during carbonated brine exposure. *Cem Concr Res*. 2018;113(May 2017):1-12. doi:10.1016/j.cemconres.2018.03.016

13. Kim S, Santamarina JC. Reactive fluid flow in CO 2 storage reservoirs: A 2-D pore network. *Greenh Gases Sci Technol*. 2015;473(5):462-473. doi:10.1002/ghg

14. Lesti M, Tiemeyer C, Plank J. CO2 stability of Portland cement based well cementing systems for use on carbon capture & storage (CCS) wells. *Cem Concr Res*. 2013;45(1):45-54. doi:10.1016/j.cemconres.2012.12.001

15. Abid K, Gholami R, Choate P, Nagaratnam BH. A review on cement degradation under CO2-rich environment of sequestration projects. *J Nat Gas Sci Eng*. 2015;27:1149-1157. doi:10.1016/j.jngse.2015.09.061

16. Teodoriu C, Bello O. A review of cement testing apparatus and methods under CO2 environment and their impact on well integrity prediction –

649 Where do we stand? *J Pet Sci Eng*. 2020;187:106736.
650 doi:10.1016/j.petrol.2019.106736

651 17. Sun X, Wu Q, Lee S, Qing Y, Wu Y. Cellulose Nanofibers as a Modifier for
652 Rheology, Curing and Mechanical Performance of Oil Well Cement. *Sci*
653 *Rep*. 2016;6:1-9. doi:10.1038/srep31654

654 18. Hisseine OA, Omran AF, Tagnit-Hamou A. Influence of cellulose filaments
655 on cement paste and concrete. *J Mater Civ Eng*. 2018;30(6):1-14.
656 doi:10.1061/(ASCE)MT.1943-5533.0002287

657 19. Hisseine OA, Wilson W, Sorelli L, Tolnai B, Tagnit-Hamou A. Nanocellulose
658 for improved concrete performance: A macro-to-micro investigation for
659 disclosing the effects of cellulose filaments on strength of cement systems.
660 *Constr Build Mater*. 2019;206:84-96. doi:10.1016/j.conbuildmat.2019.02.042

661 20. Cerrutti P, Roldán P, García RM, Galvagno MA, Vázquez A, Foresti ML.
662 Production of bacterial nanocellulose from wine industry residues:
663 Importance of fermentation time on pellicle characteristics. *J Appl Polym*
664 *Sci*. 2016;133(14). doi:10.1002/app.43109

665 21. Mejdoub R, Hammi H, Suñol JJ, Khitouni M, Boufi S. Nanofibrillated
666 cellulose as nanoreinforcement in Portland cement : Thermal , mechanical
667 and microstructural properties. *J Compos Mater*. 2017;51(17):2491-2503.
668 doi:10.1177/0021998316672090

669 22. Barría JC, Vazquez A, Pereira J, Manzanal D. Effect of bacterial
670 nanocellulose on the fresh and hardened states of oil well cement. *J Pet Sci*
671 *Eng*. 2021;In press. doi:10.1016/j.petrol.2020.108259

672 23. Hoyos CG, Zuluaga R, Gañán P, Pique TM, Vazquez A. Cellulose

673 nanofibrils extracted from fique fibers as bio-based cement additive. *J Clean*
674 *Prod*. 2019;235:1540-1548. doi:10.1016/j.jclepro.2019.06.292

675 24. Barría JC, Manzanal D, Pereira J-M, Ghabezloo S. Study on
676 poromechanical changes of nanocellulose cement composite subjected to
677 supercritical CO2. 2020.

678 25. Liu X, Falcone G, Alimonti C. A systematic study of harnessing low-
679 temperature geothermal energy from oil and gas reservoirs. *Energy*.
680 2018;142:346-355. doi:10.1016/j.energy.2017.10.058

681 26. Fabbri A, Corvisier J, Schubnel A, et al. Effect of carbonation on the hydro-
682 mechanical properties of Portland cements. *Cem Concr Res*.
683 2009;39(12):1156-1163. doi:10.1016/j.cemconres.2009.07.028

684 27. Yurtdas I, Xie SY, Burlion N, Shao JF, Saint-Marc J, Garnier A. Influence of
685 chemical degradation on mechanical behavior of a petroleum cement paste.
686 *Cem Concr Res*. 2011;41(4):412-421.
687 doi:10.1016/j.cemconres.2011.01.008

688 28. Rimmelé G, Barlet-gouédard V, Porcherie O, Goffé B, Brunet F.
689 Heterogeneous porosity distribution in Portland cement exposed to CO 2 -
690 rich fl uids. *Cem Concr Res*. 2008;38:1038-1048.
691 doi:10.1016/j.cemconres.2008.03.022

692 29. Samudio M. Modelling of an oil well cement paste from early age to
693 hardened state : hydration kinetics and poromechanical behaviour To cite
694 this version : 2018.

695 30. Charreau H, L. Foresti M, Vazquez A. Nanocellulose Patents Trends: A
696 Comprehensive Review on Patents on Cellulose Nanocrystals,

Microfibrillated and Bacterial Cellulose. *Recent Pat Nanotechnol*. 2012;7(1):56-80. doi:10.2174/18722105130106

31. API Specification 10A. *Specification for Cements and Materials for Well Cementing*. Twenty-Fif. Northwest Washington, DC; 2019. https://www.techstreet.com/standards/api-spec-10a?product_id=2038411.

32. Zeng Q, Li K, Fen-Chong T, Dangla P. Analysis of pore structure, contact angle and pore entrapment of blended cement pastes from mercury porosimetry data. *Cem Concr Compos*. 2012;34(9):1053-1060. doi:10.1016/j.cemconcomp.2012.06.005

33. Khaddour F, Grégoire D, Pijaudier-Cabot G. A Hierarchical Model for the Computation of Permeation Properties of Porous Materials and Their Enhancement due to Microcracks. *J Eng Mech*. 2018;144(2):04017160. doi:10.1061/(asce)em.1943-7889.0001392

34. Moore D, Reynolds R. *X-Ray Diffraction and the Identification and Analysis of Clay Minerals*.; 1989.

35. Biscaye PE. Geological Society of America Bulletin Mineralogy and Sedimentation of Recent Deep-Sea Clay in the Atlantic Ocean and Adjacent Seas and Oceans. *Geol Soc Am Bulletim*. 1965;76(7):803-832. doi:10.1130/0016-7606(1965)76

36. Vallin V, Pereira JM, Fabbri A, Wong H. Numerical modelling of the hydro-chemo-mechanical behaviour of geomaterials in the context of CO 2 injection. 2013;(April):3052-3069. doi:10.1002/nag

37. Vallin V. Modélisation chimio poromécanique du comportement des géomatériaux dans le contexte du stockage géologique du dioxyde de

carbone : Application au puits d'injection. 2014.

38. Manzanal D, Vallin V, Pereira JM. A chemo-poromechanical model for well/caprock interface in presence of CO2. *Poromechanics V - Proc 5th Biot Conf Poromechanics*. 2013:1470-1477. doi:10.1061/9780784412992.175

39. Fabbri A, Jacquemet N, Seyedi DM. A chemo-poromechanical model of oilwell cement carbonation under CO 2 geological storage conditions. *Cem Concr Res*. 2012;42(1):8-19. doi:10.1016/j.cemconres.2011.07.002

40. Coussy O. *Mechanics and Physics of Porous Solids*.; 2010. doi:10.1002/9780470710388

41. Ulm FJ, Constantinides G, Heukamp FH. Is concrete a poromechanics material? - A multiscale investigation of poroelastic properties. *Mater Struct Constr*. 2004;37(265):43-58. doi:10.1617/14100

42. Dangla P, Bonnard A. Ifsttar/bil: first version in github (Version v2.4). Zenodo. 2017. doi:10.5281/zenodo.1039729

43. Mainguy M. modeles de diffusion non-lineaires en milieux poreux. Applications a la dissolution et au sechage des materiaux cimentaires. 1999.

44. Ghabezloo S. Comportement thermo-poro-mécanique d'un ciment pétrolier. 2008:204.

45. Mainguy M, Coussy O. Propagation Fronts during Calcium Leaching and Chloride Penetration. *J Eng Mech*. 2000;126(3):250-257. doi:10.1061/(asce)0733-9399(2000)126:3(250)

46. Barlet-Gouedard V, Rimmelé G, Goffé B, Porcherie O. Well Technologies

744 for CO 2 Geological Storage : CO 2 -Resistant Cement. *SPE Int*.
745 2007;62(3):325-334. doi:10.2516/ogst

746 47. Kutchko BG, Strazisar BR, Dzombak DA, Lowry G V., Thauiow N.
747 Degradation of well cement by CO2 under geologic sequestration
748 conditions. *Environ Sci Technol*. 2007;41(13):4787-4792.
749 doi:10.1021/es062828c

750 48. Gu T, Guo X, Li Z, et al. Coupled effect of CO2 attack and tensile stress on
751 well cement under CO2 storage conditions. *Constr Build Mater*.
752 2017;130:92-102. doi:10.1016/j.conbuildmat.2016.10.117

753 49. Costa BL d. S, Freitas JC d. O, Melo DM d. A, Araujo RG d. S, Oliveira YH
754 d., Simão CA. Evaluation of density influence on resistance to carbonation
755 process in oil well cement slurries. *Constr Build Mater*. 2019;197:331-338.
756 doi:10.1016/j.conbuildmat.2018.11.232

757 50. Bahafid S. A multi-technique investigation of the effect of hydration
758 temperature on the microstructure and mechanical properties of cement
759 paste. 2017. https://pastel.archives-ouvertes.fr/tel-01980576.

760 51. Fu T, Montes F, Suraneni P, Youngblood J, Weiss J. The influence of
761 cellulose nanocrystals on the hydration and flexural strength of Portland
762 cement pastes. *Polymers (Basel)*. 2017;9(9). doi:10.3390/polym9090424

763 52. Cao Y, Tian N, Bahr D, et al. The influence of cellulose nanocrystals on the
764 microstructure of cement paste. *Cem Concr Compos*. 2016;74:164-173.
765 doi:10.1016/j.cemconcomp.2016.09.008

766 53. Lee HJ, Kim SK, Lee HS, Kim W. A Study on the Drying Shrinkage and
767 Mechanical Properties of Fiber Reinforced Cement Composites Using

768 Cellulose Nanocrystals. *Int J Concr Struct Mater*. 2019;13(1).
769 doi:10.1186/s40069-019-0351-2

770 54. Cao Y, Zavaterri P, Youngblood J, Moon R, Weiss J. The influence of
771 cellulose nanocrystal additions on the performance of cement paste. *Cem*
772 *Concr Compos*. 2015;56:73-83. doi:10.1016/j.cemconcomp.2014.11.008

773 55. Ecay L, Grégoire D, Pijaudier-Cabot G. On the prediction of permeability
774 and relative permeability from pore size distributions. *Cem Concr Res*.
775 2020;133(March):106074. doi:10.1016/j.cemconres.2020.106074

776 56. Melzer R, Eberhard E. Phase identification during early and middle
777 hydration of tricalciumsilicate (Ca3SiO5). *Cem Concr Res*. 1989;19(c):411-
778 422.

779 57. Sun X, Wu Q, Zhang J, Qing Y, Wu Y, Lee S. Rheology, curing temperature
780 and mechanical performance of oil well cement: Combined effect of
781 cellulose nanofibers and graphene nano-platelets. *Mater Des*. 2017;114:92-
782 101. doi:10.1016/j.matdes.2016.10.050

783 58. Akhlaghi MA, Bagherpour R, Kalhori H. Application of bacterial
784 nanocellulose fibers as reinforcement in cement composites. *Constr Build*
785 *Mater*. 2020;241:118061. doi:10.1016/j.conbuildmat.2020.118061

786 59. Jeong J, Sardini P, Ramézani H, Siitari-Kauppi M, Steeb H. Modeling of the
787 induced chemo-mechanical stress through porous cement mortar subjected
788 to CO2: Enhanced micro-dilatation theory and 14C-PMMA method. *Comput*
789 *Mater Sci*. 2013;69:466-480. doi:10.1016/j.commatsci.2012.11.031

790 60. Jang JG, Lee HK. Microstructural densification and CO2 uptake promoted
791 by the carbonation curing of belite-rich Portland cement. *Cem Concr Res*.

2016;82:50-57. doi:10.1016/j.cemconres.2016.01.001

61. Bruckdorfer RA. Carbon Dioxide Corrosion in Oilwell Cements. *Soc Pet Eng*. 1986. doi:10.2118/15176-MS

62. Sauki A, Irawan S. Effects of Pressure and Temperature on Well Cement Degradation by Supercritical CO 2. *Int J Eng Technol IJET-IJENS*. 2010;10(4):53-61.

63. Lesti M, Tiemeyer C, Plank J. CO2stability of Portland cement based well cementing systems for use on carbon capture & storage (CCS) wells. *Cem Concr Res*. 2013;45(1):45-54. doi:10.1016/j.cemconres.2012.12.001

64. Xu B, Yuan B, Wang Y, Zeng S, Yang Y. Nanosilica-latex reduction carbonation-induced degradation in cement of CO2 geological storage wells. *J Nat Gas Sci Eng*. 2019;65(February):237-247. doi:10.1016/j.jngse.2019.03.013

65. Costa BL de S, Freitas JC de O, Santos PHS, Melo DM de A, Araujo RG da S, de Oliveira YH. Carbonation in oil well Portland cement: Influence of hydration time prior to contact with CO2. *Constr Build Mater*. 2018;159:252-260. doi:10.1016/j.conbuildmat.2017.10.103

66. Morandeau A, Thiéry M, Dangla P. Impact of accelerated carbonation on OPC cement paste blended with fly ash. *Cem Concr Res*. 2015;67:226-236. doi:10.1016/j.cemconres.2014.10.003

67. Ershadi, V., Ebadi, E., Rabani, A. R., Ershadi, L., & Soltanian H. Reduction of set cement permeability in oil well to decrease the pollution of receptive environment using spherical nanosilica. In: *2nd International Conference on Environmental Science and Technology*. Vol 6. ; 2011:101-104.

68. Krakowiak KJ, Thomas JJ, Musso S, James S, Akono A, Ulm F. Cement and Concrete Research Nano-chemo-mechanical signature of conventional oil-well cement systems : Effects of elevated temperature and curing time. *Cem Concr Res*. 2015;67:103-121. doi:10.1016/j.cemconres.2014.08.008

69. Neves A, Romildo J, Toledo D, Jo F. A study of CO2 capture by high initial strength Portland cement pastes at early curing stages by new non-conventional thermogravimetry and non-conventional differential thermal analysis. *J Therm Anal Calorim*. 2017. doi:10.1007/s10973-017-6326-0

70. Ghabezloo S, Sulem J, Saint-Marc J. Evaluation of a permeability-porosity relationship in a low-permeability creeping material using a single transient test. *Int J Rock Mech Min Sci*. 2009;46(4):761-768. doi:10.1016/j.ijrmms.2008.10.003

71. Bahafid S, Ghabezloo S, Duc M, Faure P, Sulem J. Effect of the hydration temperature on the microstructure of Class G cement: C-S-H composition and density. *Cem Concr Res*. 2017;95:270-281. doi:10.1016/j.cemconres.2017.02.008

72. Sercombe J, Galle C. Rehydration and microstructure of cement paste after heating at temperatures up to 300 ° C. 2003;33:1047-1056. doi:10.1016/S0008-8846(03)00005-X

73. Ghabezloo S. Cement and Concrete Research Effect of the variations of clinker composition on the poroelastic properties of hardened class G cement paste. *Cem Concr Res*. 2011;41(8):920-922. doi:10.1016/j.cemconres.2011.03.022

74. Mainguy M, Mod MM. Mod ` eles de diffusion non lin ´ eaire en milieux

poreux . Applications a la dissolution et au s ´ echage des mat ´ eriaux cimentaires. 1999.

75. Huet B, Tasoti V, Khalfallah I. Energy Procedia A review of Portland cement carbonation mechanisms in CO 2 rich environment . *Energy Procedia*. 2011;4:5275-5282. doi:10.1016/j.egypro.2011.02.507

76. Shen J. Reactive transport modeling of CO2 through cementitious materials under CO2 geological storage conditions. 2013.

77. Kutchko BG, Strazisar BR, Lowry GV, Dzombak D a., Thaulow N. Rate of CO2 Attack on Hydrated Class H Well Cement under Geologic Sequestration Conditions. *Environ Sci \& Technol*. 2008;42(16):6237–6242. doi:10.1021/es800049r

78. Morandeau A, Thiéry M, Dangla P. Investigation of the carbonation mechanism of CH and C-S-H in terms of kinetics, microstructure changes and moisture properties. *Cem Concr Res*. 2014;56:153-170. doi:10.1016/j.cemconres.2013.11.015

Table Captions

Table 1. MIP Tests

Table 2. Density and mass uptake after carbonation

Table 3. Intrinsic permeabilities

Table 4. Relative percentage of the crystalline phases before and after exposure

Table 5. Elastic properties measured by elastic waves velocities Vp and Vs

Table 6. Initial medium conditions for simulations

Table 7. Molar Volumes in cm^3/mol

Table 8. Initial conditions for the downhole simulation

Table 9. Values of κ for different values of κ_0

Table 10. Values of deff for different values of $d_{eff,0}$

Table 1. MIP Tests

Test	Reference	Curing temperature [°C]	BNC [%]	Carbonation days	Porosity [%]
1	PC-Reference	90	0	0	33.7
2	PC-NC	90	0	0	34.6
3	BNC05-NC	90	0.05	0	34.5
4	PC-30INT	90	0	30	24.5
5	PC-30EXT	90	0	30	21.5
6	BNC05-30INT	90	0.05	30	23.2
7	BNC05-30EXT	90	0.05	30	21.0

Table 2. Density and mass uptake after carbonation

Samples (III)		Initial density [g/cm3]	Final density [g/cm3]	Mass gained [%]
1	PC	1.89	2.14	13.5%
2	PC	1.89	2.15	13.5%
3	PC	1.89	2.13	12.4%
4	PC	1.89	2.15	13.4%
5	BNC05	1.87	2.12	13.5%
6	BNC05	1.87	2.13	13.7%
7	BNC05	1.88	2.12	12.6%
8	BNC05	1.87	2.09	11.8%

Table 3. Intrinsic permeabilities

Sample	k [m^2]
PC - NC	$3.4.10^{-18}$
PC - C	$3.1.10^{-19}$
BNC05 - NC	$3.2.10^{-19}$
BNC05 - C	$2.6.10^{-19}$

Table 4. Relative percentage of the crystalline phases before and after exposure

Crystalline phase (%)	PC Sample		0.05 sample	
	SC	C	SC	C
Porlandite	32	1	33	-

Katoite	28	-	29	-
Magnesite	10	-	5	-
Brownmillerite	16	6	15	7
Calcite	14	43	18	44
Aragonite	-	50	-	49

Table 5. Elastic properties measured by elastic waves velocities Vp and Vs

Sample	G [GPa]	K [GPa]	E [GPa]	ν
PC - NC	8.4	9.5	19.5	0.16
PC - C	8.9	12.7	21.3	0.22
BNC05 - NC	7.8	8.5	18	0.15
BNC05 - C	8.9	9.8	20.5	0.15

Table 6. Initial medium conditions for simulations

η_{vis} [MPa.s]	K_F [MPa]	ρ_F [kg/m³]	R_c [MPa]	R_t [MPa]
0.5 10^{-9}	2200	1000	24	2.4

Table 7. Molar Volumes in cm³/mol

ν^S_{CH}	$\nu^S_{C-S-H_{1.6}}$	$\nu^S_{CaCO_3}$	$\nu^S_{SiO_2(H_2O)_{0.5}}$	$\nu^F_{H_2O}$
33.1	84.7	36.9	31	18.85

Table 8. Initial conditions for the downhole simulation

Inclusion	Volumetric prop. PC-BNC	Bulk modulus [GPa]	Shear modulus [GPa]
Porosity	0.345	-	-
CH	0.18	33.00	14.50
C-S-H	0.405	25.00	18.40
Aluminates	0.06942	27.00	9.50
Calcite	0.00	69.00	37.40
BNC	0.00058	42.00	38.00

Table 9. Values of κ for different values of κ_0

Porosity	Parameter κ_0 [m²]					
	0.1	1	10	100	350	500
0.325	2.24E-19	2.24E-18	2.24E-17	2.24E-16	7.86E-16	1.12E-15

Table 10. Values of d_{eff} for different values of $d_{eff,0}$

Porosity	Parameter $d_{eff,0}$ [m²/s]					
	0.1	1	10	100	160	300
0.325	7.27E-13	7.27E-12	7.27E-11	7.27E-10	1.16E-9	2.18E-9

Figure Captions

Fig. 1. Carbonation equipment used

Fig. 2. Samples cured at 90 °C and carbonated for 30 days (PC and BNC05)

Fig. 3. Pore size distribution variation of oven-dried and non-oven-dried samples

Fig. 4. Pore size distribution of carbonated and non-carbonated PC samples

Fig. 5. Pore size distribution of carbonated and non-carbonated BNC05 samples

Fig. 6. XRD patterns of non-modified cement (PC) and modified cement (BNC05) before carbonation (NC) and after carbonation (C)

903 **Fig. 7.** Compressive strength and Young's Moduli variation after carbonation of PC and BNC05
904 samples
905 **Fig. 8.** 2D model. Representation of one-quarter sample subjected to carbonation using the code
906 BIL
907 **Fig. 9.** Left: Results of the simulation showing the variation of porosity in the experimental BNC05
908 sample of 38mm by 78 mm for values of κ_0 = 350 and $d_{eff,0}$ = 160. Right: Results of porosity in 1D
909 **Fig. 10.** Dissolution and carbonation fronts development over time
910 **Fig. 11.** Permeability variation over time of an annular cement thickness of ¾ inch
911 **Fig. 12.** Volumetric proportions after 15 and 30 days of carbonation of an annular cement thickness
912 of ¾ inch
913

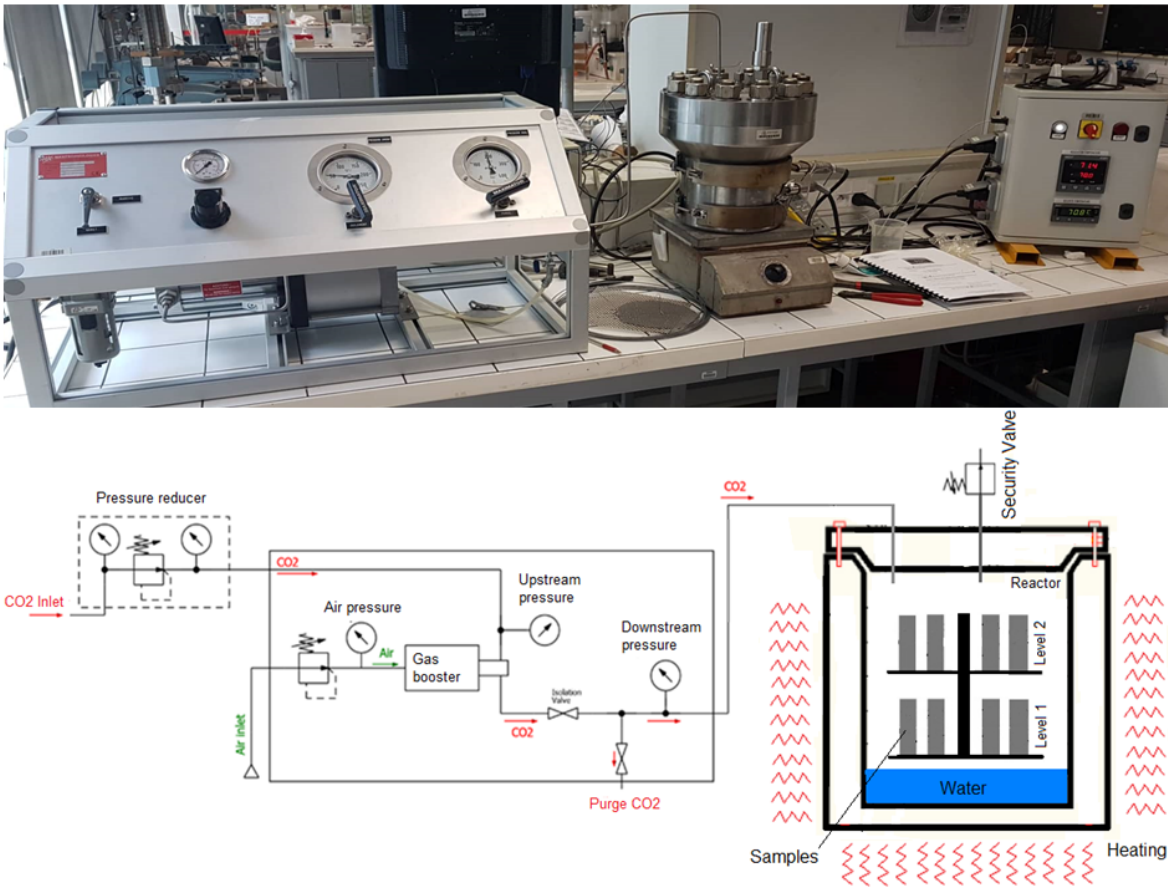

914
915 **Fig. 1.** Carbonation equipment used

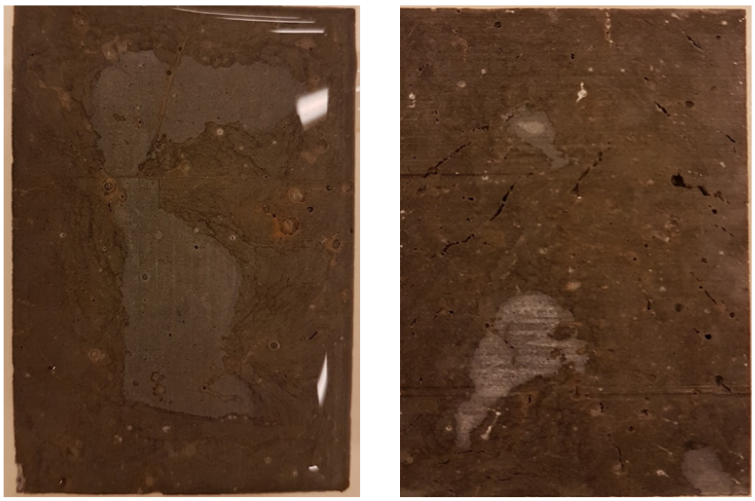

Fig. 2. Samples cured at 90°C and carbonated for 30 days (PC and BNC05)

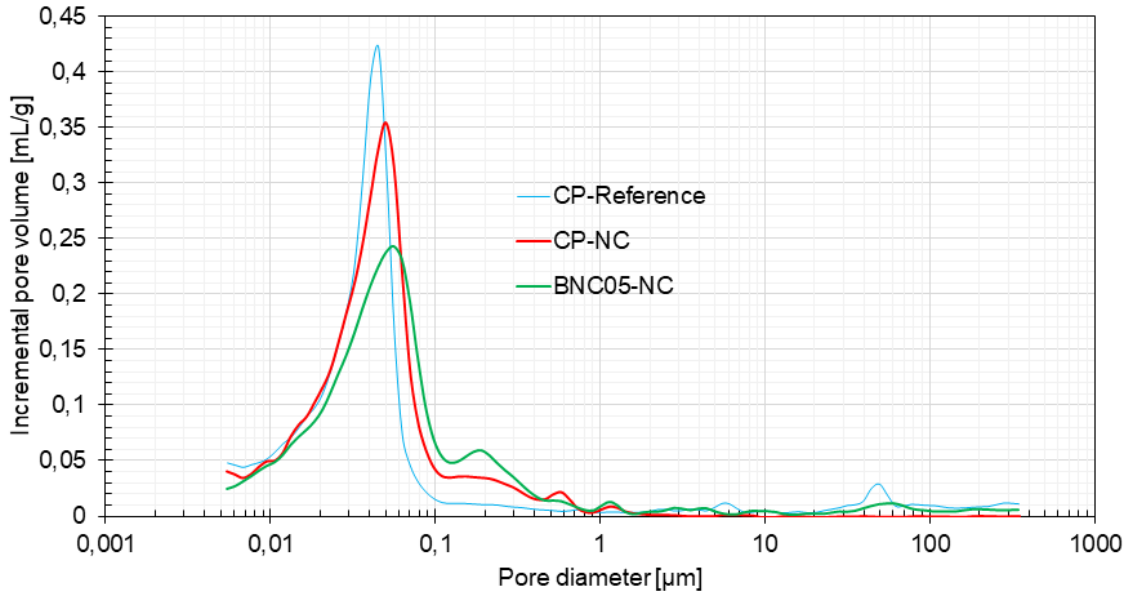

Fig. 3. Pore size distribution variation of oven-dried and non-oven-dried samples

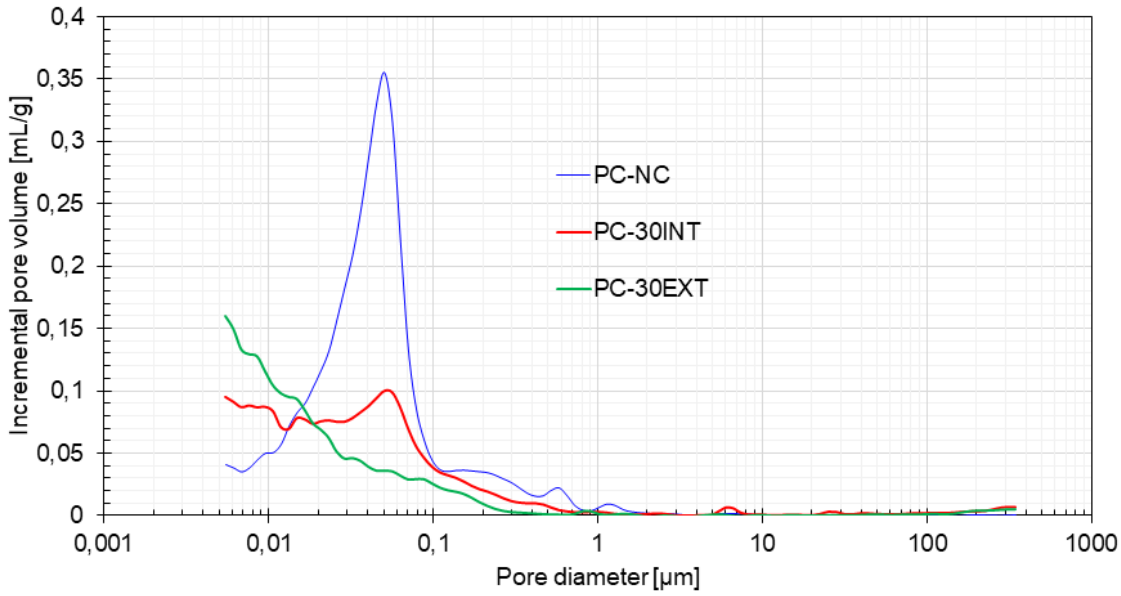

920

921 **Fig. 4.** Pore size distribution of carbonated and non-carbonated PC samples

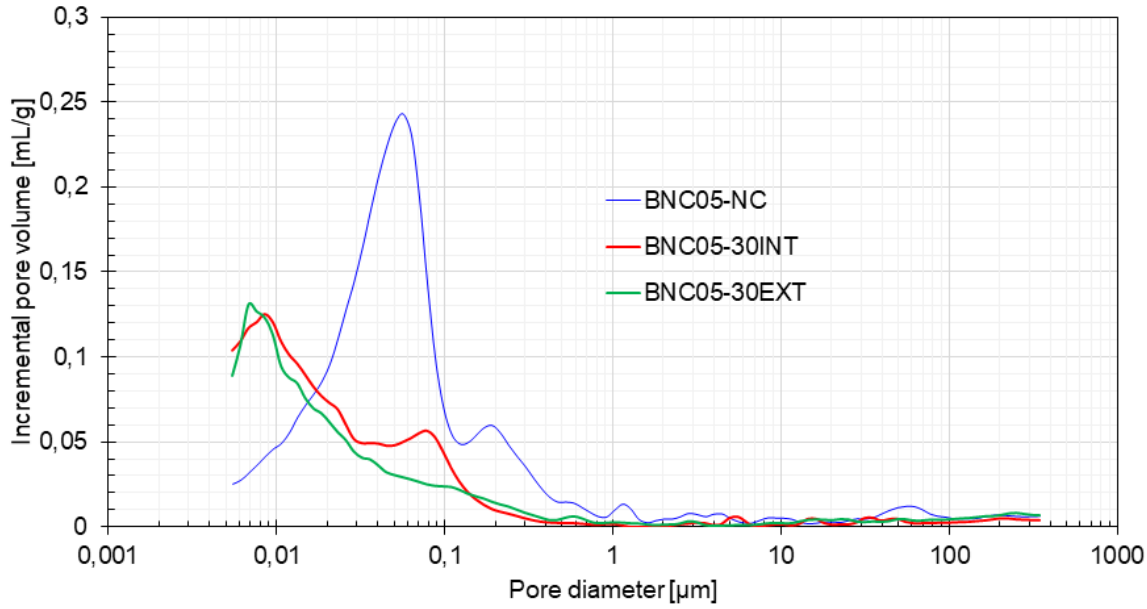

922

923 **Fig. 5.** Pore size distribution of carbonated and non-carbonated BNC05 samples

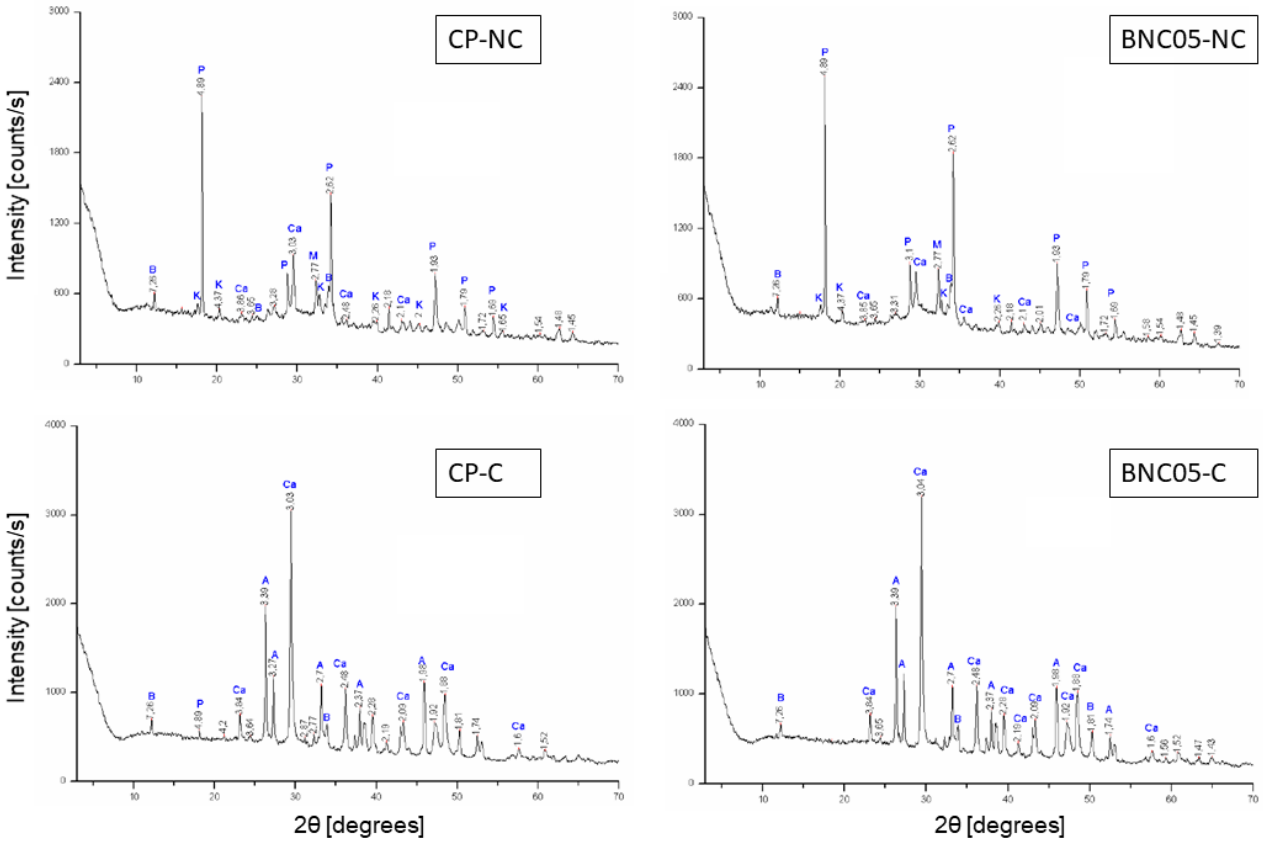

924

925 **Fig. 6.** XRD patterns of non-modified cement (PC) and modified cement (BNC05) before

926 carbonation (NC) and after carbonation (C)

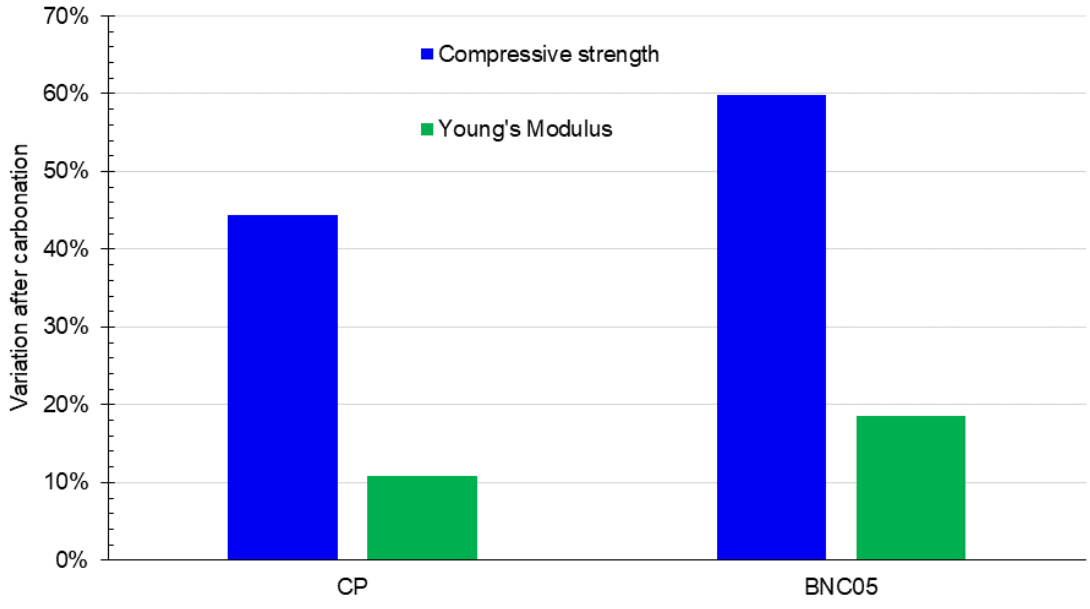

927

928 **Fig. 7.** Compressive strength and Young's Moduli variation after carbonation of PC and BNC05

929 samples

930

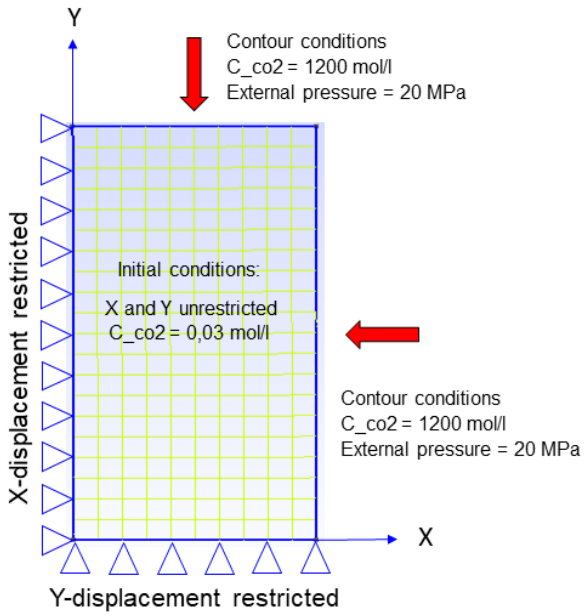

Fig. 8. 2D model. Representation of one-quarter sample subjected to carbonation using the code BIL

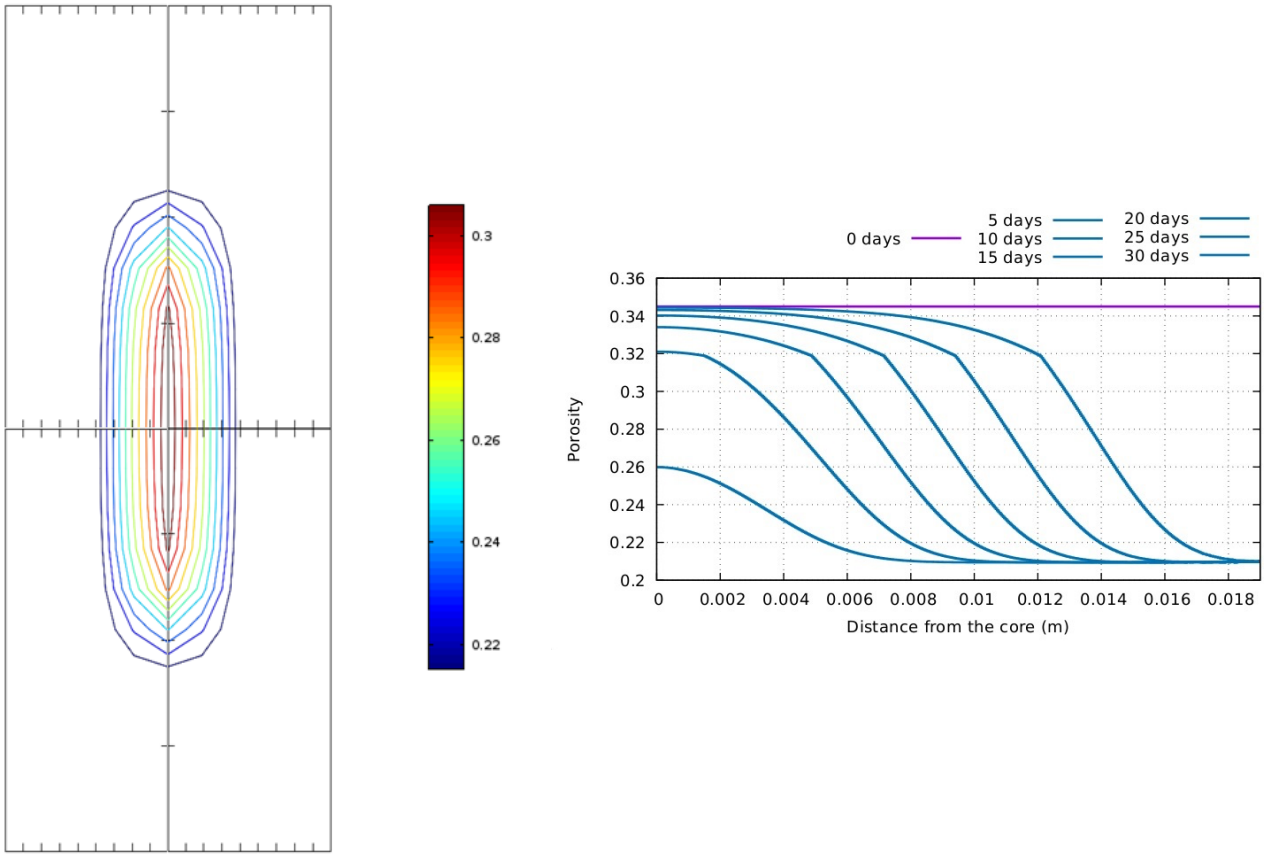

Fig. 9. Left: Results of the simulation showing the variation of porosity in the experimental BNC05 sample of 38mm by 78 mm for values of κ_0 = 350 and $d_{eff,0}$ = 160. Right: Results of porosity in 1D over the sample radius.

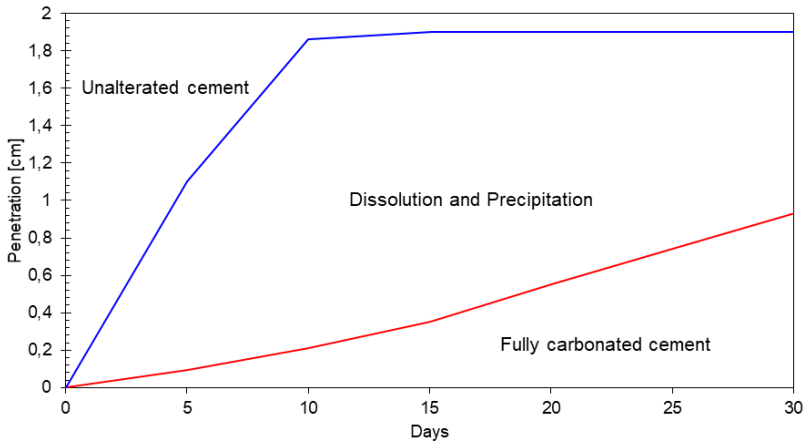

938

939 **Fig. 10.** Dissolution and carbonation fronts development over time

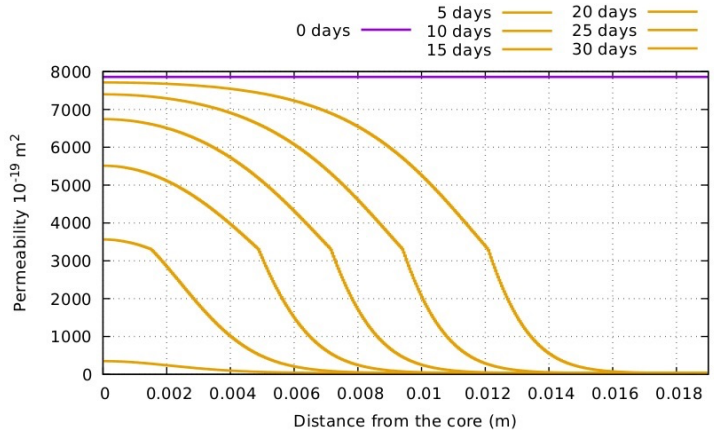

940

941 **Fig. 11.** Permeability variation over time of an annular cement thickness of ¾ inch

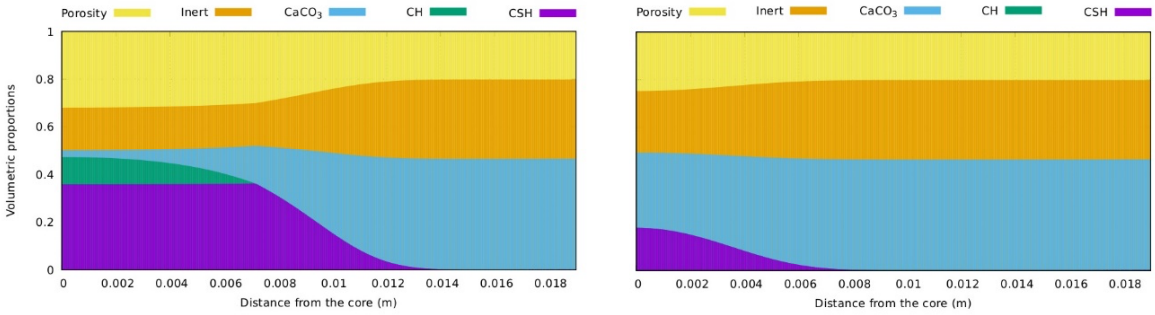

942

943 **Fig. 12.** Volumetric proportions after 15 and 30 days of carbonation of an annular cement

944 thickness of ¾ inch